JFM RAPIDS
journals.cambridge.org/rapids

Dissolution instability and roughening transition

Philippe Claudin[1,†], **Orencio Durán**[2] **and Bruno Andreotti**[3]

[1]Physique et Mécanique des Milieux Hétérogènes, UMR 7636 ESPCI – CNRS –
Univ. Paris-Diderot – Univ. P. M. Curie, 10 rue Vauquelin, 75005 Paris, France

[2]Department of Ocean Engineering, Texas A & M University, College Station,
TX 77843-3136, USA

[3]Laboratoire de Physique Statistique, UMR 8550 Ecole Normale Supérieure – CNRS –
Univ. Paris-Diderot – Univ. P. M. Curie, 24 rue Lhomond, 75005 Paris, France

We theoretically investigate the pattern formation observed when a fluid flows over
a solid substrate that can dissolve or melt. We use a turbulent mixing description
that includes the effect of the bed roughness. We show that the dissolution instability
at the origin of the pattern is associated with an anomaly at the transition from a
laminar to a turbulent hydrodynamic response with respect to the bed elevation.
This anomaly, and therefore the instability, disappears when the bed becomes
hydrodynamically rough, above a threshold roughness-based Reynolds number. This
suggests a possible mechanism for the selection of the pattern amplitude. The most
unstable wavelength scales as observed in nature on the thickness of the viscous
sublayer, with a multiplicative factor that depends on the dimensionless parameters
of the problem.

Key words: morphological instability, pattern formation, turbulent transition

1. Introduction

Pattern formation often occurs in nature when a fluid, flowing above a solid
bed, can erode or transport some material of the bed. This mass transfer can be,
for example, associated with sediment transport, as for sand ripples and dunes
(Charru, Andreotti & Claudin 2013). It can also be of thermodynamical origin, with
melting, sublimation or dissolution of the bed (Meakin & Jamtveit 2010), which
this paper is devoted to. This occurs, for instance, in cave conduits, where the
limestone dissolves in the water flow, forming scallops (Blumberg & Curl 1974; Curl
1974; Thomas 1979). Similar scallop patterns form on meteorites with regmaglypts

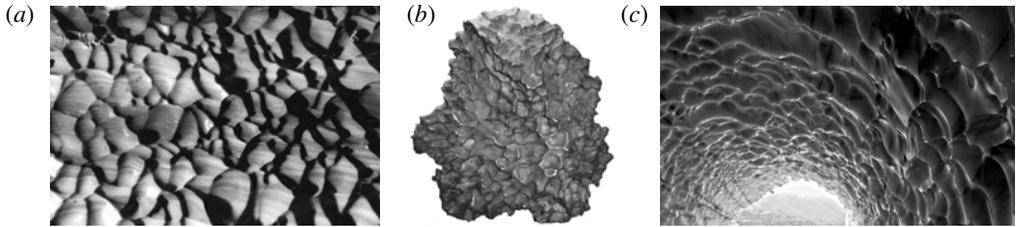† Email address for correspondence: philippe.claudin@espci.fr

(*a*) (*b*) (*c*)

FIGURE 1. Pictures showing scallops (*a*) on marble (Korallgrottan cave; photo width $\simeq 0.5$ m), (*b*) at the surface of a meteorite (Cabin Creek meteorite; width $\simeq 0.4$ m) and (*c*) on ice (tunnel in Tarfala Valley; largest scallops $\simeq 1$ m).

(Lin & Qun 1986; Claudin & Ernstson 2004), on glaciers and snow fields with suncups and ablation hollows (Rhodes, Armstrong & Warren 1987; Herzfeld *et al.* 2003), at the surface of firn walls and caves and icebergs (Sharp 1947; Leighly 1948; Richardson & Harper 1957; Kiver & Mumma 1971; Anderson *et al.* 1998; Cohen *et al.* 2016) or in steel pipes under the action of corrosion (Lister *et al.* 1998; Villen, Zheng & Lister 2001). Water flows on ice can also produces ripples (Carey 1966; Ashton & Kennedy 1972; Gilpin, Hirata & Cheng 1980; Gilpin 1981; Ogawa & Furukawa 2002), in particular on icicles (Ueno & Farzaneh 2011; Chen & Morris 2013). Other related studies concern the shape evolution of dissolving objects (Nakouzi, Goldstein & Steinbock 2014; Huang, Moore & Ristroph 2015) or the emergence of precipitation patterns in geothermal hot springs (Goldenfeld, Chan & Veysey 2006). A few examples are shown in figure 1.

In all of these situations, the flow is influenced by the bed elevation or profile, and, in turn, erosion or transport induced by the flow makes the solid surface evolve. This feedback loop can lead to an instability, where bed perturbations are amplified. Several linear stability analyses have been performed for these dissolution/melting problems, in order to compute the growth rate of a perturbation of given wavenumber k and determine the selected most unstable mode (Hanratty 1981; Ogawa & Furukawa 2002; Ueno & Farzaneh 2011; Camporeale & Ridolfi 2012). In this paper, building on the pioneering work of Hanratty (1981), we incorporate the effect of the bed roughness in the hydrodynamical description, which is absent of previous analyses. This roughness turns out to be of key importance, as the dissolution instability is found to disappear when the bed becomes rough; that is, above a threshold corresponding to a value of the roughness-based Reynolds number. We hypothesise that this restabilisation may explain the amplitude selection of the pattern.

The model proposed in this paper is composed of several parts. The first one, independent of the dissolution problem, deals with the description of a turbulent flow over a solid surface, using a turbulent closure relating the stresses to the velocity gradient (§ 2). We use here a standard mixing length approach, with two specificities: we incorporate the role of the surface roughness and that of the pressure gradient on the turbulent mixing. Dissolution or melting is described by means of the advection–diffusion of a passive scalar (§ 3) that can represent the temperature or the concentration of a dissolved species. It is coupled to the hydrodynamical part mainly because the coefficient of diffusion is related to the turbulent mixing. To address the development of an instability leading to the emergence of dissolution bedforms, we investigate this model in the case of a sinusoidally perturbed surface. The equations

are linearised in the limit of a small perturbation and coupled to an erosion law for the bed evolution to derive the dispersion relation of the problem (§ 4). It provides the growth rate and propagation velocity of the perturbation, and thus fully characterises the instability. Finally, the results are presented and discussed in § 5, and compared with experimental data.

2. Reynolds averaged description and turbulent closure

We consider a fluid flow along the x direction over a bed of elevation denoted by Z. Here, z is the crosswise axis normal to the main bed and y is spanwise. Following the standard separation between average quantities and fluctuating ones (denoted by a prime), the equations governing the mean velocity field u_i and the pressure p can be written as

$$\partial_i u_i = 0 \quad \text{and} \quad \rho \partial_t u_i + u_j \partial_j u_i = \partial_j \tau_{ij} - \partial_i p, \qquad (2.1a,b)$$

where τ_{ij} contains the Reynolds stress tensor $-\rho \overline{u_i' u_j'}$. Here, ρ is the density of the fluid, assumed to be constant. We use a first-order turbulence closure to relate the stress to the velocity gradient. It involves a turbulent viscosity resulting from the product of a mixing length and a mixing frequency, representing the typical eddy length and time scales (Pope 2000). The mixing length ℓ depends explicitly on the distance from the bed. The mixing frequency is given by the strain rate modulus $|\dot{\gamma}| = \sqrt{1/2 \dot{\gamma}_{ij} \dot{\gamma}_{ij}}$, where we have introduced the strain rate tensor $\dot{\gamma}_{ij} = \partial_i u_j + \partial_j u_i$. In a homogeneous situation along the x-axis, the strain rate reduces to $\partial_z u_x$. For a constant shear stress associated with a shear velocity u_*, we write

$$\tau_{xz} = \rho \ell^2 |\partial_z u_x| \partial_z u_x + \rho \nu \partial_z u_x = \rho |u_*| u_*, \qquad (2.2)$$

where ν is the kinematic fluid viscosity. In order to account for both smooth and rough regimes, we adopt here a van Driest-like mixing length (Pope 2000),

$$\ell = \kappa (z + rd - Z) \left[1 - \exp \left(-\frac{(\tau_{xz}/\rho)^{1/2}(z + sd - Z)}{\nu \mathcal{R}_t} \right) \right]. \qquad (2.3)$$

In this expression, $\kappa = 0.4$ is the von Kármán constant, d is the sand equivalent bed roughness size and $\mathcal{R}_t$ is the van Driest transitional Reynolds number, equal to $\mathcal{R}_t^0 \simeq 25$ in the homogeneous case of a flat bed (Pope 2000). The exponential term suppresses turbulent mixing within the viscous sublayer, close enough to the bed, $z = Z$. The dimensionless numbers $r = 1/30$ and $s = 1/3$ are calibrated with measurements of velocity profiles over varied rough walls (Schultz & Flack 2009; Flack & Schultz 2010). Here, rd corresponds to the standard Prandtl hydrodynamical roughness extracted by extrapolating the logarithmic law of the wall at vanishing velocity. On the other hand, and this is more original, sd controls the reduction of the viscous layer thickness upon increasing the bed roughness.

Following the work of Hanratty (1981), $\mathcal{R}_t$ cannot be taken as constant but depends on a dimensionless number $\mathcal{H}$ that lags behind the pressure gradient following a relaxation equation,

$$a \frac{\nu}{u_*} \partial_x \mathcal{H} = \frac{\nu}{u_*^3} \partial_x (\tau_{xx} - p) - \mathcal{H}, \qquad (2.4)$$

where a is the multiplicative factor in front of the space lag. We also introduce $b = 1/\mathcal{R}_t^0 d\mathcal{R}_t/d\mathcal{H} > 0$ as the relative variation of $\mathcal{R}_t$ due to the pressure gradient. The values of these empirical parameters have been set to $a = 2000$ and $b = 35$, as
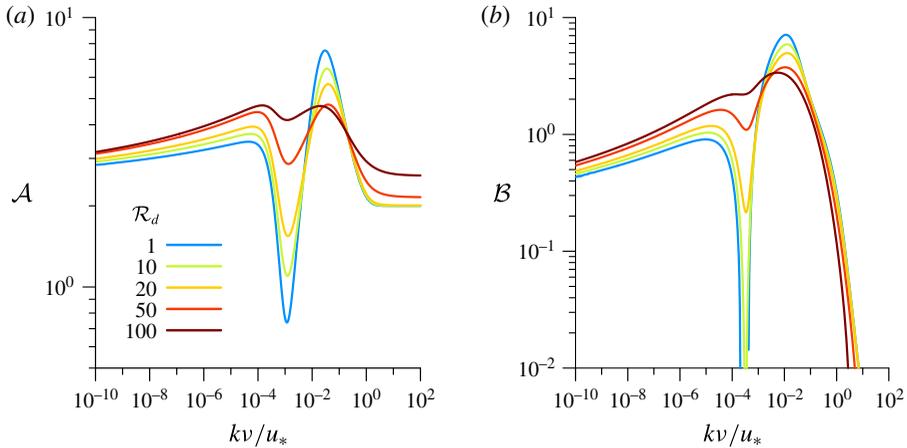
FIGURE 2. Basal shear stress coefficients (*a*) $\mathcal{A}$ and (*b*) $\mathcal{B}$ computed by the model as functions of $k\nu/u_*$. The different colours code for the value of the parameter $\mathcal{R}_d$ (see legend). The laminar–turbulent transition (around $k\nu/u_* \simeq 10^{-3}$) gradually disappears when $\mathcal{R}_d$ increases.

calibrated on the behaviour of the basal shear stress over a modulated bed (Charru *et al.* 2013). Their values control the amplitude and location of the anomaly at the transition from a laminar to a turbulent response with respect to the bed elevation, as illustrated below.

We shall focus here on quasi two-dimensional situations, i.e. on geometries invariant along the *y* direction. This simplification is a limitation for the study of non-transverse patterns, such as these scallops which have a kind of chevron shape, but is certainly enough to capture the physics of the instability. We can generally write the stress tensor as

$$\tau_{ij} = \rho(\ell^2|\dot{\gamma}| + \nu)\dot{\gamma}_{ij} - \tfrac{1}{3}\rho\chi^2\ell^2|\dot{\gamma}|^2\delta_{ij}, \tag{2.5}$$

where δ_{ij} is the Kronecker symbol (see Fourrière, Claudin & Andreotti (2010) and references therein). The typical value of the phenomenological constant χ is in the range 2–3, but is of no importance here as we shall see that only the normal stress difference $\tau_{xx} - \tau_{zz}$ matters. This closed model allows us to compute the velocity and stress profiles for given boundary conditions, as illustrated in §4.

Before addressing the linear stability analysis, it is useful to discuss and show the effect of the bed roughness on the hydrodynamical quantities, here taking the shear stress as a typical example. Anticipating §4, where a sinusoidally modulated bed $Z(x) = \zeta e^{ikx}$ of wavenumber *k* is considered, these hydrodynamical equations can be linearised with respect to the small parameter $k\zeta$. In this case, the shear stress is also modulated and correspondingly takes the generic form $\tau_{xz} = \rho u_*^2(1 + k\zeta e^{ikx}S_t) + \text{c.c.}$, where $S_t(\eta)$ is a dimensionless function of the rescaled vertical coordinate $\eta = kz$. We define the two coefficients $\mathcal{A}$ and $\mathcal{B}$ by $S_t(0) = \mathcal{A} + i\mathcal{B}$; these are computed as outputs of the hydrodynamic model. The basal shear stress is then a sinusoidal function of *x* and these coefficients encode the in-phase and in-quadrature components in response to the bed modulation. The coefficients $\mathcal{A}$ and $\mathcal{B}$ are functions of *k*, as displayed in figure 2. The main point, which is the hydrodynamical novelty of this study, is that they are also found to strongly depend on the bed roughness-based Reynolds number $\mathcal{R}_d = du_*/\nu$. As described and discussed by Charru *et al.* (2013), these

coefficients present, in the smooth limit ($\mathcal{R}_d < 1$), a marked transition between the turbulent regime associated with small wavenumbers $kv/u_* \lesssim 10^{-4}$ and the laminar regime, typically for $kv/u_* \gtrsim 10^{-2}$. This transition, evidenced by the experimental data of Hanratty and his co-workers (Zilker, Cook & Hanratty 1977; Frederick & Hanratty 1988), resembles a 'crisis', with sharp variations of $\mathcal{A}$ and $\mathcal{B}$, allowing, in particular, for negative values of $\mathcal{B}$. The coefficients a and b introduced above have been adjusted to fit these data (Charru *et al.* 2013). Crucially, this transition progressively disappears upon increasing the roughness Reynolds number, recovering the reference rough behaviour above $\mathcal{R}_d \gtrsim 100$ (Fourrière *et al.* 2010). Beyond the phenomenology, a detailed physical understanding of this laminar–turbulent transition remains a pending hydrodynamical open problem.

3. Scalar transport

We wish now to describe a passive scalar ϕ, e.g. the concentration of a chemical species or the temperature, which is transported by the flow. We model its dynamics by a simple advection–diffusion equation,

$$\partial_t \phi + \partial_x q_x + \partial_z q_z = 0, \tag{3.1}$$

where the flux $\boldsymbol{q}$ is the sum of a convective and a diffusive term, $\boldsymbol{q} = \phi \boldsymbol{u} - D \boldsymbol{\nabla} \phi$. Here, we take a diffusion coefficient proportional to the turbulent viscosity and write

$$D = \frac{\ell^2 |\dot{\gamma}|}{\beta_t} + \frac{\nu}{\beta_\nu}, \tag{3.2}$$

where β_t and β_ν are the turbulent and viscous Schmidt numbers (or Prandtl numbers for temperature), here taken as constants. A typical value for liquids as well as gasses is $\beta_t = 0.7$ (Gualtieri *et al.* 2017). For the molecular diffusivity, β_ν can be estimated from the Stokes–Einstein relation, $\nu/\beta_\nu = k_B T/6\pi \rho \nu r_m$, where k_B is the Boltzmann constant, T is the temperature and r_m is the molecular effective radius. The order of magnitude of molecular diffusion for ions or for dissolved CO_2 in water is $\beta_\nu = 10^3$; for the diffusion of particles in an ideal gas, a typical value is $\beta_\nu = 1$.

In the base state for which the bed is homogeneous in x, we can assume that the solid bed dissolves or melts at a small constant velocity and then perform the computation in the moving frame of reference. Equation (3.1) reduces to $\partial_z q_z = 0$, so that the flux is constant,

$$q_z = -D \partial_z \phi = q_0. \tag{3.3}$$

With the above expression (3.2) for D, we obtain the equation for the vertical profile of the scalar field ϕ,

$$\left(\frac{\ell^2 |\dot{\gamma}|}{\beta_t} + \frac{\nu}{\beta_\nu} \right) \partial_z \phi = -q_0. \tag{3.4}$$

To solve this equation, a condition on the bed must be specified. It depends on the nature of the scalar field, but can be formally written in a unique general way. For thermal problems, we impose the bed temperature, $\phi_0 = T_0$. For dissolution or sublimation problems, we write a Hertz–Knudsen type of law (Eames, Marr & Sabir 1997), with a flux of matter that depends on the concentration at the surface,

$$q_0 = \alpha(\phi_{sat} - \phi_0). \tag{3.5}$$

Because this condition applies on the bed, where the velocity vanishes, no convective contribution to the flux is involved. In the above expression, ϕ_{sat} is the concentration at

saturation, and α is a reaction kinetic constant, here expressed as a velocity scale. For simplicity, we take it constant. In the case of sublimation or evaporation, α is given by the thermal velocity times a desorption probability (Eames *et al.* 1997), leading to α in the range 1–10 m s^{-1}. In dissolution problems, however, we expect α to take much smaller values, of the order of 10^{-5} m s^{-1} (Falter, Atkinson & Coimbra 2005). Equation (3.5) can be re-expressed as $\phi_0 = \phi_{sat} - q_0/\alpha$, so that in both cases ϕ_0 is given. Finally, as buoyancy effects are usually negligible in such problems, we consider that the momentum equation is not coupled to the scalar field.

4. Linearised equations

We can now proceed to the linear stability analysis, to compute the dispersion relation.

4.1. *Definitions and base state*

For small enough amplitudes, we can consider a bottom profile of the form

$$Z(x) = \zeta e^{ikx} \tag{4.1}$$

without loss of generality (real parts of expressions are understood). Here, $\lambda = 2\pi/k$ is the wavelength of the bottom and ζ is the amplitude of the corrugation. The case of an arbitrary relief can be deduced by a simple superposition of Fourier modes. We introduce the dimensionless variable $\eta = kz$, $\eta_0 = kd$ and the wavenumber-based Reynolds number $\mathcal{R} = u_*/k\nu$. Primed quantities in this section denote derivatives with respect to η. With these notations and following (2.3), the mixing length in the base state can be expressed in a dimensionless form as

$$k\ell \equiv \Upsilon(\eta) = \kappa(\eta + r\eta_0)(1 - \exp(-\mathcal{R}(\eta + s\eta_0)/\mathcal{R}_t^0)). \tag{4.2}$$

We define the function $\mathcal{U}(\eta)$ giving the wind profile in the base state as $u_x \equiv u_*\mathcal{U}$. From (2.2), we see that it must verify the following equation:

$$\Upsilon^2|\mathcal{U}'|\mathcal{U}' + \mathcal{R}^{-1}\mathcal{U}' = 1, \quad \text{or equivalently} \quad \mathcal{U}' = \frac{-1 + \sqrt{1 + 4\Upsilon^2\mathcal{R}^2}}{2\Upsilon^2\mathcal{R}}, \tag{4.3a,b}$$

which must be solved with the boundary condition $\mathcal{U}(0) = 0$ corresponding to the no-slip condition of the wind at the solid interface. Similarly, we define the function $\mathcal{P}(\eta)$ for the passive scalar in the base state as $\phi - \phi_0 \equiv q_0\mathcal{P}/u_*$. From (3.4), it obeys

$$\left(\frac{\Upsilon^2|\mathcal{U}'|}{\beta_t} + \frac{\mathcal{R}^{-1}}{\beta_\nu}\right)\mathcal{P}' + 1 = 0. \tag{4.4}$$

The boundary condition is $\mathcal{P}(0) = 0$, corresponding to the condition $\phi = \phi_0$ on the bed.

4.2. *Linear expansion*

The aim of this subsection is to derive a set of closed equations (4.11)–(4.16), which, once integrated with given boundary conditions, provide as outputs the basal stresses, scalar concentration and flux, in order to compute the dispersion relation of the problem. Although technical, the principle of the calculation is simple and relies on the linearisation of the governing equations with respect to the small parameter $k\zeta$, which is proportional to the aspect ratio of the bed modulation. As in Fourrière *et al.* (2010), all quantities are generically written as the sum of their homogeneous term

(along x) plus a linear correction generically written as $ck\zeta e^{ikx}C(\eta)$. The scaling factor c encodes the physical dimension, whereas C is a non-dimensional mode function which describes the vertical profile of the correction. Scaling velocities with u_* and stresses with ρu_*^2, we define the mode functions $U(\eta)$ and $W(\eta)$ for u_x and u_z, and the functions $S_t(\eta)$, $S_n(\eta)$, $S_{xx}(\eta)$ and $S_{zz}(\eta)$ for τ_{xz}, $p - \tau_{zz}$, τ_{xx} and τ_{zz} respectively. For the dimensionless mixing length $k\ell$, we write its mode function L. The scalar concentration is scaled by q_0/u_* and its mode function is Φ; its flux is scaled by q_0 and its mode function is defined as $-F$. Finally, we call Δ the mode function of the coefficient of diffusion. These functions are not all independent, and with these notations, we can in particular express the coefficient of diffusion as

$$D = \frac{u_*}{k}\left[\left(\frac{\mathcal{U}'\Upsilon^2}{\beta_t} + \frac{\mathcal{R}^{-1}}{\beta_v}\right) + \frac{1}{\beta_t}[(U' + iW)\Upsilon^2 + 2\Upsilon L\mathcal{U}']k\zeta e^{ikx}\right]. \tag{4.5}$$

Following (2.5), we express the stress functions as follows:

$$S_t = (\mathcal{R}^{-1} + 2\Upsilon^2\mathcal{U}')(U' + iW) + 2\Upsilon\mathcal{U}'^2L, \tag{4.6}$$

$$S_{xx} - S_{zz} = 4(\mathcal{R}^{-1} + \Upsilon^2\mathcal{U}')iU = \frac{4iU}{\mathcal{U}'}, \tag{4.7}$$

where we have used $(\mathcal{R}^{-1} + \Upsilon^2\mathcal{U}') = 1/\mathcal{U}'$ at the zeroth order (equation (4.3)). Linearising the Hanratty equation (2.4), one obtains

$$(\mathcal{R} + ia)\mathcal{H} = i(S_{xx} - S_{zz} - S_n) = -\frac{4U}{\mathcal{U}'} - iS_n. \tag{4.8}$$

The linear expansion of the scalar equation gives

$$F' = i\mathcal{P}U + \left(i\mathcal{U} + \frac{\Upsilon^2|\mathcal{U}'|}{\beta_t} + \frac{\mathcal{R}^{-1}}{\beta_v}\right)\Phi, \tag{4.9}$$

with $\quad F = \left(\frac{\Upsilon^2|\mathcal{U}'|}{\beta_t} + \frac{\mathcal{R}^{-1}}{\beta_v}\right)\Phi' + \frac{1}{\beta_t}\mathcal{P}'\left[\Upsilon^2(U' + iW) + 2\Upsilon L\mathcal{U}'\right] - W\mathcal{P}. \tag{4.10}$

Combining these equations with the linearised Navier–Stokes equations, we finally obtain six closed equations,

$$U' = -iW + \frac{S_t - 2\Upsilon\mathcal{U}'^2L}{\mathcal{R}^{-1} + 2\Upsilon^2\mathcal{U}'}, \tag{4.11}$$

$$W' = -iU, \tag{4.12}$$

$$S_t' = \left(i\mathcal{U} + \frac{4}{\mathcal{U}'}\right)U + \mathcal{U}'W + iS_n, \tag{4.13}$$

$$S_n' = -i\mathcal{U}W + iS_t, \tag{4.14}$$

$$\Phi' = \left[F + W\mathcal{P} - \frac{\mathcal{P}'\left(\Upsilon^2S_t + 2\Upsilon L\mathcal{U}'\left(\mathcal{R}^{-1} + \Upsilon^2\mathcal{U}'\right)\right)}{\beta_t\left(\mathcal{R}^{-1} + 2\Upsilon^2\mathcal{U}'\right)}\right] \Bigg/ \left[\frac{\Upsilon^2|\mathcal{U}'|}{\beta_t} + \frac{\mathcal{R}^{-1}}{\beta_v}\right], \tag{4.15}$$

$$F' = i\mathcal{P}U + \left(i\mathcal{U} + \frac{\Upsilon^2|\mathcal{U}'|}{\beta_t} + \frac{\mathcal{R}^{-1}}{\beta_v}\right)\Phi, \tag{4.16}$$

where the disturbance to the rescaled mixing length reads

$$L = \kappa\left\{-1 + e^{-(\mathcal{R}/\mathcal{R}_t^0)(\eta + s\eta_0)}\left[1 - \frac{\mathcal{R}}{\mathcal{R}_t^0}(\eta + r\eta_0)\right.\right.$$
$$\left.\left. + \frac{\mathcal{R}}{\mathcal{R}_t^0}(\eta + s\eta_0)(\eta + r\eta_0)\left(\frac{1}{2}S_t + \frac{b}{\mathcal{R} + ia}\left(\frac{4U}{\mathcal{U}'} + iS_n\right)\right)\right]\right\}. \tag{4.17}$$

4.3. *Boundary conditions*

Six boundary conditions must be specified to solve the system (4.11)–(4.16), labelled (i)–(vi) below. The upper boundary corresponds to the limit $\eta \to \infty$, in which the vertical fluxes of mass and momentum vanish asymptotically. This means that the first-order corrections to the shear stress and to the vertical velocity must tend to zero: (i) $W(\infty) = 0$ and (ii) $S_t(\infty) = 0$. In practice, we introduce a finite height H (or $\eta_H \equiv kH$) at which we impose a null vertical velocity and a constant tangential stress $-\rho u_*^2$, so that $W(\eta_H) = 0$ and $S_t(\eta_H) = 0$. Then, we consider the limit $H \to +\infty$, i.e. when the results become independent of H. On the bed, $z = Z$, both velocity components must vanish, which gives (iii) $U(0) = -\mathcal{U}'(0)$ and (iv) $W(0) = 0$. Using (4.3) and (4.2), we can express

$$U(0) = \frac{1 - \sqrt{1 + 4\Upsilon(0)^2 \mathcal{R}^2}}{2\Upsilon(0)^2 \mathcal{R}} = \frac{1 - \sqrt{1 + 4[\kappa r \eta_0 (1 - \exp(-s\eta_0 \mathcal{R}/\mathcal{R}_t^0))]^2 \mathcal{R}^2}}{2[\kappa r \eta_0 (1 - \exp(-s\eta_0 \mathcal{R}/\mathcal{R}_t^0))]^2 \mathcal{R}}. \quad (4.18)$$

Regarding the passive scalar, we hypothesise that its flux through the upper boundary remains constant, which gives (v) $F(\eta_H) = 0$. Finally, on the bed, the dissolution-like condition $q_z = \alpha(\phi_{sat} - \phi)$, associated with its zeroth order (3.5), leads to (vi) $F(0) = \alpha/u_*[\mathcal{P}'(0) + \Phi(0)]$, where $\mathcal{P}'(0)$ is known from (4.4). Other quantities like $S_t(0)$ and $S_n(0)$ come as results of the calculation.

As both $F(0)$ and $\phi(0)$ must remain bounded to be compatible with the bulk equations, we expect two simple asymptotic regimes: in the limit of small α/u_*, the scalar modulation $\Phi(0)$ results from the mixing of the base profile and is independent of α; the flux modulation $F(0)$ follows and must vanish linearly in α/u_*. Conversely, at large α/u_*, the situation is opposite: the substrate is so erodible that any disturbance in concentration at the surface would lead to a diverging flux resorbing it. As $\Phi(0)$ vanishes as u_*/α, the flux $F(0)$ results from the mixing of the base state and is therefore constant.

4.4. *Interface growth rate*

To compute the temporal evolution of the bed elevation, we proceed with $Z(x, t) = \zeta e^{\sigma t + i\omega t + ikx}$, where $\sigma(k)$ is the growth rate and $\omega(k)$ is the angular frequency of the bed pattern along x. The phase propagation speed is therefore $-\omega/k$ with these notations. As the equations are linear in ϕ, one can always define the relevant scalar with the appropriate factor so that the evolution equation for the bottom reads $\partial_t Z = q_0 - q_z(Z)$. At the linear order, this gives the dispersion relation,

$$\sigma + i\omega = q_0 k F(0). \quad (4.19)$$

5. Results and discussion

The dispersion relation (4.19) is displayed in figure 3, in the limit of small α/u_* and at vanishing $\mathcal{R}_d$ (smooth case). Following the asymptotic behaviour of $F(0)$ in this limit, the relevant rescaling factor for σ is $q_0 \alpha/\nu$. We see in (*a*) a range of unstable wavenumbers with a positive growth rate, in which σ reaches a maximum value σ_m at k_m. In this range, the propagation velocity changes sign (*b*), showing that the instability is absolute and not convective. As shown in figure 4(*a*), the key result is that the unstable band disappears above a critical value $\mathcal{R}_c$ of the roughness Reynolds number.
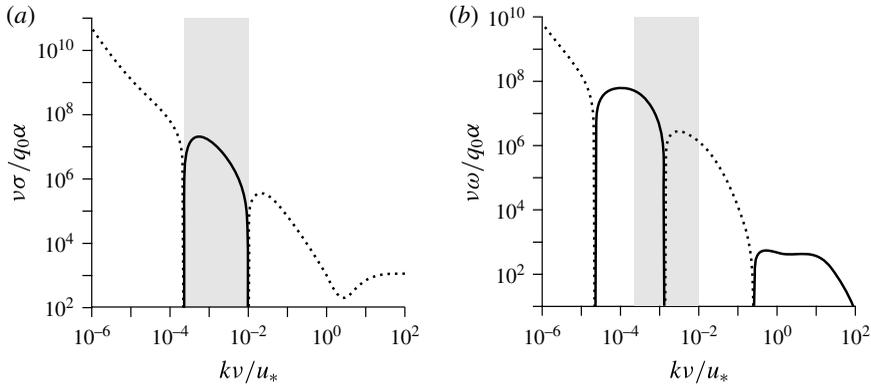
FIGURE 3. The dispersion relation for the dissolution instability in the limit of small α/u_*, for $\beta_v = 10^3$ and $\mathcal{R}_d = 10$. (a) Growth rate σ. (b) Angular frequency ω. Solid lines represent positive values. For negative values, $-\sigma$ or $-\omega$ is plotted (dotted lines). The grey region corresponds to the unstable ($\sigma > 0$) range of wavenumbers.
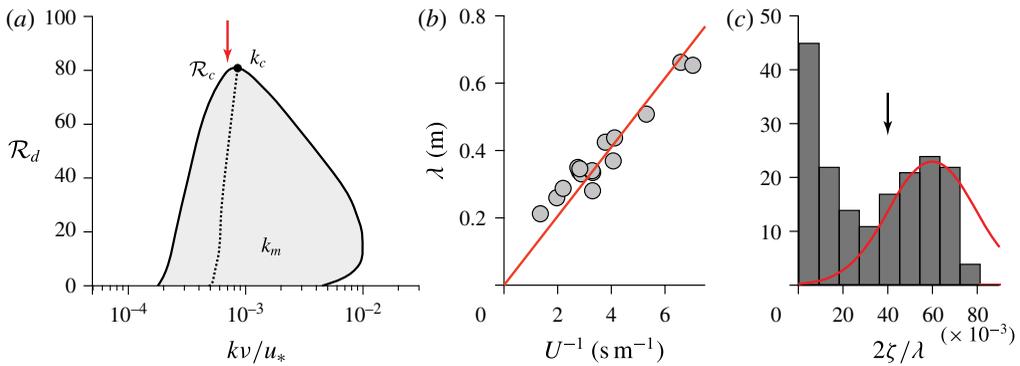

FIGURE 4. (a) Stability diagram in the plane $(\mathcal{R}_d, k\nu/u_*)$, computed in the limit of small α/u_* and for $\beta_v = 10^3$. Solid line: marginal stability curve ($\sigma = 0$). Grey: unstable zone ($\sigma > 0$). Dotted line: location of the most unstable modes (σ_m). (b) Experimental data of Ashton & Kennedy (1972) on ice ripples: mean wavelength versus inverse of mean flow velocity. The linear fit $\lambda \simeq 0.1/U$ (solid line) corresponds to the red arrow in (a). (c) Histogram of the ripple aspect ratio in these experiments. The black arrow corresponds to the aspect ratio giving $\mathcal{R}_d = \mathcal{R}_c$.

As illustrated in figure 5, one can understand the instability mechanism as follows. The erosion of the bed is driven by the mass flux q_z, itself controlled by the concentration gradient and the coefficient of diffusion (equation (3.3)). The concentration profile, enforced by the base state, is non-homogeneous, decreasing away from the surface. The crests of a modulated bed profile come closer to regions of lower concentration, enhancing the gradient with respect to the surface where ϕ is imposed. For a constant D, this peak effect increases the flux and thus the erosion at the crests, and this stabilising situation is what happens at large $k\nu/u_*$, when the wavelength is much smaller than the viscous sublayer. When turbulence is dominant, D is not constant any more, but is controlled by turbulent mixing.
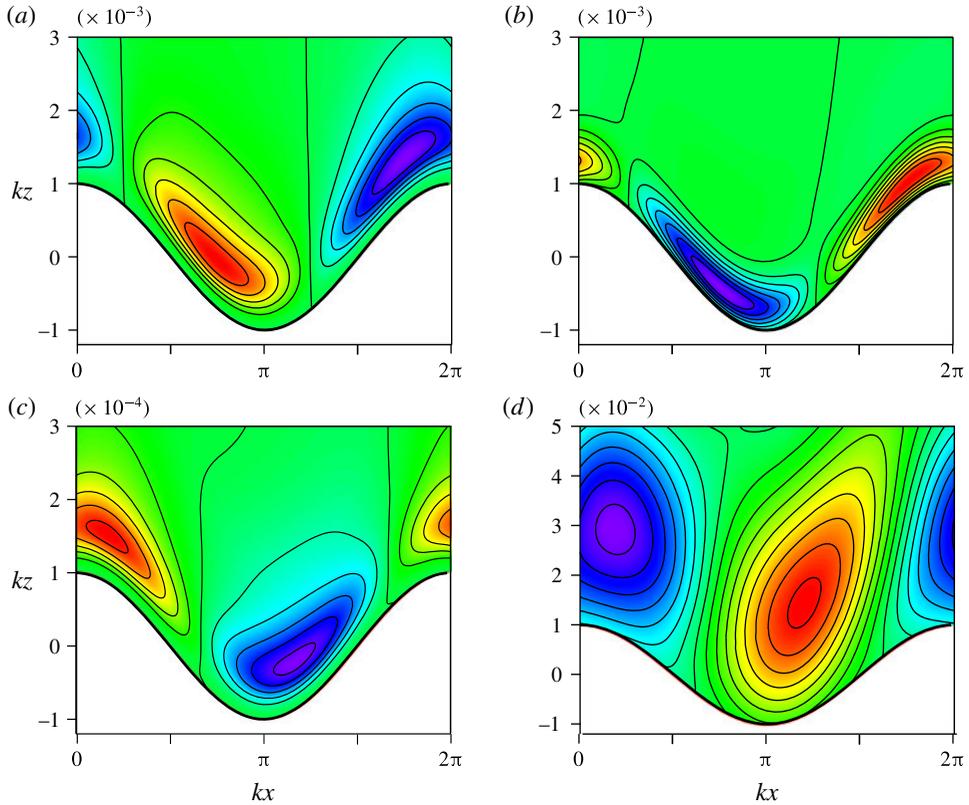
FIGURE 5. (*a*) Isocontours of the diffusion coefficient above a modulated bed (in white), with a wavenumber close to the most unstable mode, $k\nu/u_* = 5 \times 10^{-4}$. The other parameter values are $\mathcal{R}_d = 0.1$, $\alpha/u_* = 0.01$, $\eta_H = 10$ and $\beta_\nu = 10^3$. Red (blue) regions correspond to a strong (weak) mixing. (*b*) Corresponding isocontours of the concentration ϕ. Strong mixing leads to a large vertical flux which reduces ϕ. (*c*) The same as (*a*), but for a smaller wavenumber, $k\nu/u_* = 5 \times 10^{-5}$. (*d*) Isocontours of the concentration ϕ at a larger wavenumber, $k\nu/u_* = 5 \times 10^{-2}$. In all panels, the flow is from left to right.

At small $k\nu/u_*$, turbulence is enhanced slightly upstream of the crests, and hence there is stabilising erosion again. For wavenumbers in the intermediate range corresponding to the laminar–turbulent transition, however, turbulence is shifted downstream by means of the adverse pressure gradient (2.4), enhancing mixing and thus erosion in the troughs, which a is destabilising (amplifying) situation. The opposite behaviour of the in-phase modulations of D and ϕ is displayed in figure 6 for the whole range of wavenumbers, showing a change of sign corresponding to enhanced mixing in troughs in the presence of the laminar–turbulent transition only.

   Changing the molecular diffusivity, this phenomenology with a range of unstable modes (figure 4*a*) remains, but with consequently varying values of $\mathcal{R}_c$ and k_c (figure 7*a*). For $\mathcal{R}_c$, we clearly identify a low-β_ν regime where $\mathcal{R}_c \propto 1/\beta_\nu$ and a plateau at large β_ν. This means that diffusive processes are controlled by whatever is dominant between the diffusion of momentum (ν) and that of dissolved species (ν/β_ν). Moreover, k_c is found to be pretty constant, independent of β_ν, with a typical value of around $10^{-3}u_*/\nu$. This relative invariance is what one can expect for a
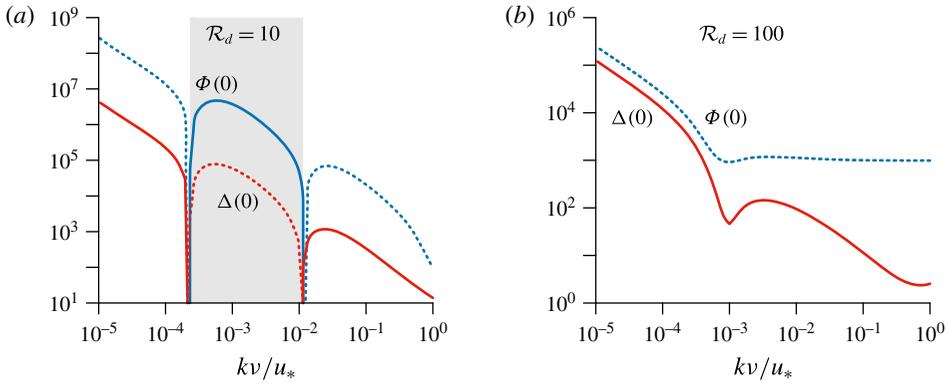
FIGURE 6. In-phase components of the modulation of the diffusion coefficient $\Delta(0)$ in red and of the basal concentration $\Phi(0)$ in blue, for $\mathcal{R}_d = 10$ (*a*) and $\mathcal{R}_d = 100$ (*b*), as functions of $k\nu/u_*$. Dashed lines represent negative values. The grey region is the unstable range of wavenumbers.
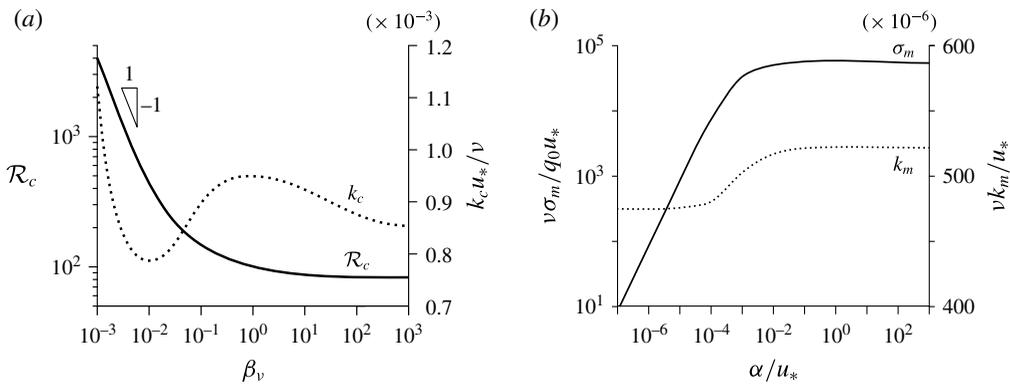

FIGURE 7. (*a*) Critical value $\mathcal{R}_c$, at which the instability disappears, as a function of β_ν (solid line, left axis), in the limit of small α/u_*. Right axis, dotted line: corresponding critical wavenumber k_c. (*b*) Maximum growth rate (solid line, left axis) and corresponding wavenumber (dotted line, right axis) as functions of α/u_*, computed for $\beta_\nu = 10^3$ and $\mathcal{R}_d \to 0$.

bandpass instability. Exploring a broad range of the ratio α/u_* in figure 7(*b*), but now rescaling the growth rate by $q_0 u_*/\nu$, we see that σ_m becomes independent of it, with a crossover at around $\alpha/u_* \simeq 10^{-3}$. These regimes correspond to those discussed for $F(0)$, in relation to (4.19). Meanwhile, the most unstable wavenumber k_m switches from a plateau value to another value, with a small relative change, emphasising again that relevant wavenumbers are fairly insensitive to all parameters.

The development of the instability actually increases the bed roughness, suggesting that the pattern eventually selects the wavenumber k_c nonlinearly. As a matter of fact, converting the amplitude of the bed perturbation to a sand equivalent roughness size d (Flack & Schultz 2010), the value $\mathcal{R}_d \simeq 80$ is reached with a pattern aspect ratio $2\zeta/\lambda$ of the order of 5 % for these values of k, i.e. typically $k\zeta \simeq 0.16$. This value is clearly the upper bound for the linear expansion to make sense, but still reasonably small.

P. Claudin, O. Durán and B. Andreotti

Thomas ([1979](#)) has gathered measurements from various experiments that provide evidence of the global scaling of the selected scallop wavenumber with the viscous length. The fit of these data gives $k \simeq 6 \times 10^{-3} u_*/\nu$. This is in fair agreement with our results, but to be more quantitative, we must emphasise two difficulties when looking in more detail at specific experiments. A first ambiguity lies in the definition of the wavelength for three-dimensional objects like scallops. For example, in the study of a dissolution pattern on plaster by Blumberg & Curl ([1974](#)), λ is identified as the ratio $\langle \Lambda^3 \rangle / \langle \Lambda^2 \rangle$, where the angle brackets denote an average over measurements of longitudinal scallop sizes Λ. With this definition, a selected wavenumber $k \simeq 3 \times 10^{-3} u_*/\nu$ is reported. Another issue in computing the value of $k\nu/u_*$ from experimental data is the difficulty of relying on an accurate estimate of the shear velocity, as also discussed by Blumberg & Curl ([1974](#)). Usually, the mean flow velocity is actually measured, and u_* is computed assuming a velocity profile, typically the logarithmic law of the wall, which leads to $u_* \simeq \kappa U / \ln H/z_0$, where H is the flow depth and z_0 is the hydrodynamical roughness, itself related to the bedform amplitude as $z_0 = rd$.

Closer to the two-dimensional situation that we consider here, we have more quantitatively investigated the data of Ashton & Kennedy ([1972](#)) for ice ripples. These authors report a clear linear law, $\lambda \sim 1/U$ (figure [4b](#)). They have also measured the ripple aspect ratio. This quantity is widely distributed (figure [4c](#)), showing a population of emerging bedforms with small aspect ratios, and another one of mature ripples, with an aspect ratio centred around 6 % (figure [4c](#)). Computing u_* from U as discussed above, we obtain for these data $k\nu/u_* \simeq 8 \times 10^{-4}$, in quantitative agreement with the value of k_c (figure [4a](#)). Further experimental studies are needed to investigate the emergence and development of this instability in more detail, and in particular to follow the evolution of the bed roughness over time (Villen, Zheng & Lister [2005](#)). Another direction of research is the investigation of fast flows in order to connect scallops generated by water flows with those on meteorites, for which supersonic effects are expected.

Acknowledgements

References

ANDERSON, C. H., BEHRENS, C. J., FLOYD, G. A. & VINING, M. R. 1998 Crater firn caves of Mount St. Helens, Washington. *J. Cave Karst Studies* **60**, 44–50.

ASHTON, G. D. & KENNEDY, J. F. 1972 Ripples on the underside of river ice covers. *J. Hydraul. Div. ASCE* **98**, 1603–1624.

BLUMBERG, P. N. & CURL, R. L. 1974 Experimental and theoretical studies of dissolution roughness. *J. Fluid Mech.* **65**, 735–751.

CAMPOREALE, C. & RIDOLFI, L. 2012 Ice ripple formation at large Reynolds numbers. *J. Fluid Mech.* **694**, 225–251.

CAREY, K. L. 1966 Observed configuration and computed roughness of the underside of river ice, St Croix River, Wisconsin. *US Geol. Survey Prof. Paper* **550**, B192–B198.

CHARRU, F., ANDREOTTI, B. & CLAUDIN, P. 2013 Sand ripples and dunes. *Annu. Rev. Fluid Mech.* **45**, 469–493.

CHEN, A. S.-H. & MORRIS, S. W. 2013 On the origin and evolution of icicle ripples. *New J. Phys.* **15**, 103012.

CLAUDIN, F. & ERNSTSON, K. 2004 Regmaglypts on clasts from the Puerto Mínguez ejecta, Azuara multiple impact event (Spain). From www.impact-structures.com/article%20text.pdf.

COHEN, C., BERHANU, M., DERR, J. & COURRECH DU PONT, S. 2016 Erosion patterns on dissolving and melting bodies. *Phys. Rev. Fluids* **1**, 050508.

CURL, R. L. 1974 Deducing flow velocity in cave conduits from scallops. *NSS Bull.* **36**, 1–5.

EAMES, I. W., MARR, N. J. & SABIR, H. 1997 The evaporation coefficient of water: a review. *Intl J. Heat Mass Transfer* **40**, 2963–2973.

FALTER, J. L., ATKINSON, M. J. & COIMBRA, C. F. M. 2005 Effects of surface roughness and oscillatory flow on the dissolution of plaster forms. *Limnol. Oceanogr.* **50**, 246–254.

FLACK, K. A. & SCHULTZ, M. P. 2010 Review of hydraulic roughness scales in the fully rough regime. *Trans. ASME J. Fluids Engng* **132**, 041203.

FOURRIÈRE, A., CLAUDIN, P. & ANDREOTTI, B. 2010 Bedforms in a turbulent stream: formation of ripples by primary linear instability and of dunes by nonlinear pattern coarsening. *J. Fluid Mech.* **649**, 287–328.

FREDERICK, K. A. & HANRATTY, T. J. 1988 Velocity measurements for a turbulent non-separated flow over solid waves. *Exp. Fluids* **6**, 477–486.

GILPIN, R. R. 1981 Ice formation in a pipe containing flows in the transition and the turbulent regimes. *Trans. ASME J. Heat Transfer* **103**, 363–368.

GILPIN, R. R., HIRATA, T. & CHENG, K. C. 1980 Wave formation and heat transfer at an ice–water interface in the presence of a turbulent flow. *J. Fluid Mech.* **99**, 619–640.

GOLDENFELD, N., CHAN, P. Y. & VEYSEY, J. 2006 Dynamics of precipitation pattern formation at geothermal hot springs. *Phys. Rev. Lett.* **96**, 254501.

GUALTIERI, C., ANGELOUDIS, A., BOMBARDELLI, F., JHA, S. & STOESSER, T. 2017 On the values for the turbulent Schmidt number in environmental flows. *Fluids* **2**, 17.

HANRATTY, T. J. 1981 Stability of surfaces that are dissolving or being formed by convective diffusion. *Annu. Rev. Fluid Mech.* **13**, 231–252.

HERZFELD, U. C., MAYER, H., CAINE, N., LOSLEBEN, M. & ERBRECHT, T. 2003 Morphogenesis of typical winter and summer snow surface patterns in a continental alpine environment. *Hydro. Proces.* **17**, 619–649.

HUANG, J. M., MOORE, M. N. J. & RISTROPH, L. 2015 Shape dynamics and scaling laws for a body dissolving in fluid flow. *J. Fluid Mech.* **765**, R3.

KIVER, E. P. & MUMMA, M. D. 1971 Summit firn caves, Mount Rainier, Washington. *Science* **173**, 320–322.

LEIGHLY, J. 1948 Cuspate surfaces of melting ice and firn. *Geograph. Rev.* **38**, 301–306.

LIN, T. C. & QUN, P. 1986 On the formation of regmaglypts on meteorites. *Fluid Dyn. Res.* **1**, 191–199.

LISTER, D. H., GAUTHIER, P., GOSZCZYNSKI, J. & SLADE, J. 1998 The accelerated corrosion of CANDU primary piping. In *Proceedings Japan Atomic Indus. Forum Int. Conf. on Water Chemistry in Nuclear Power Plants*, 442.

MEAKIN, P. & JAMTVEIT, B. 2010 Geological pattern formation by growth and dissolution in aqueous systems. *Proc. R. Soc. Lond.* A **466**, 659.

NAKOUZI, E., GOLDSTEIN, R. E. & STEINBOCK, O. 2014 Do dissolving objects converge to a universal shape? *Langmuir* **31**, 4145.

OGAWA, N. & FURUKAWA, Y. 2002 Surface instability of icicles. *Phys. Rev.* E **66**, 041202.

POPE, S. B. 2000 *Turbulent Flows*. Cambridge University Press.

RHODES, J. J., ARMSTRONG, R. L. & WARREN, S. G. 1987 Mode of formation of ablation hollows controlled by dirt content of snow. *J. Glaciol.* **33**, 135–139.

RICHARDSON, W. E. & HARPER, R. D. M. 1957 Ablation polygons on snow – further observations and theories. *J. Glaciol.* **3**, 25–27.

SCHULTZ, M. P. & FLACK, K. A. 2009 Turbulent boundary layers on a systematically varied rough wall. *Phys. Fluids* **21**, 015104.

SHARP, R. P. 1947 The Wolf Creek Glaciers, St. Elias Range, Yukon Territory. *Geograph. Rev.* **37**, 26–52.

THOMAS, R. M. 1979 Size of scallops and ripples by flowing water. *Nature* **277**, 281–283.

UENO, K. & FARZANEH, M. 2011 Linear stability analysis of ice growth under supercooled water film driven by a laminar airflow. *Phys. Fluids* **23**, 042103.

VILLEN, B., ZHENG, Y. & LISTER, D. H. 2001 The scalloping phenomenon and its significance in flow-assisted corrosion. In *Proceedings 26th Annual CNS–CNA Student Conf., Toronto*.

VILLEN, B., ZHENG, Y. & LISTER, D. H. 2005 Surface dissolution and the development of scallops. *Chem. Engng Commun.* **192**, 125–136.

ZILKER, D. P., COOK, G. W. & HANRATTY, T. J. 1977 Influence of the amplitude of a solid wavy wall on a turbulent flow. Part 1. Non-separated flows. *J. Fluid Mech.* **82**, 29–51.